Chapter 5

MODEL DEVELOPMENT II

Sand tests

In Chapter 4 the shear strength of ice rubble was analyzed using regression techniques. The strength was shown to be a complex function of confinement stress which is inseparable from block size in the reported laboratory results. Varying experimental techniques, and the correlation of many experimental conditions distort the relative importance of control variables and underscore the need for direct field measurement of parametric inputs in force prediction models.

Structure interaction experiments were also reviewed in Chapter 4. For most combinations of data sets, interaction forces were shown to be strongly related to hydrostatic earth pressure. For the trials involving the data sets reviewed in Chapter 3 it was shown that the only parameters with significant influence on interaction force were rubble depth, weight and structure diameter. Again the problem of correlated variables was prevalent as rubble strength could be defined by rubble depth, ridge width by ridge depth *etc.*.

In this chapter an attempt is made to decipher the composition of the proportionality coefficients for the force models in Chapter 4. Experiments have been conducted using piles of dry sand that model, in inverted form, a rubble ice keel. It is conjectured in this study that the plastic deformation of "sand keels" in the laboratory may provide a simple

but effective analogue for natural ridge failure processes. Though no scaling of loads is intended, the "sand keel" approach sheds light on fundamental failure mechanisms and force trends for the indentation of keel-like accumulations of a granular material. The ease and simplicity of systematic testing with sand is in sharp contrast to experimenting with floating ice rubble in the lab. Sand also has roughly the same lower bound shear strength as ice rubble and the literature points out that failure modes in soils are not significantly influenced by cohesion. In the present chapter, a load model is developed for vertical and sloped structures in sand providing a basis for understanding the results in Chapter 4.

5.1 Keel replication experiments

5.1.1 Introduction

In this section experiments are described in which ice rubble keels created in the IMD laboratory using the "dumptruck" technique in McKenna *et al.* (1995b) (reported in Section 3.4) are replicated with sand and indented at reduced scale. The purpose is two-fold: to compare force patterns so that ice rubble indentation force can be contrasted against a purely frictional material, and, to justify the use of sand as a substitute for ice rubble in experiments where elucidating general failure patterns and load trends are the objectives. Only the submerged portions of the ridges interacting with the cylindrical part of the structure in McKenna (1995b) are considered in this study.

Figure 5.1 is a plot of laboratory ice rubble shear data from Chapter 4. The theoretical behaviour of a loose and dense sand (from Bowles, 1984) and plastic blocks (from Urroz

and Ettema, 1987) is shown for comparison. The figure indicates that the lower bound strength (or weakest state) of ice rubble undergoing shear is similar to that of loose sand. As described earlier, the scatter in the upper portion is attributable to various degrees of inter-block bonding or rubble *cohesion*. The absence of cohesion in sand tests is not expected to adversely influence the applicability of experimental results. Jumakis (1984) states, "Consideration of stress condition in soil shows that cohesion of a ϕ-c soil does not affect the position of the rupture surface.". Also, in the study of soil failure in front of tines it has been observed that rupture distance (leading extent of failure pattern) is substantially independent of cohesion (Osman, 1964) and moisture content in sand (Rajaram and Oida, 1992).

5.1.2 Experimental program

The keel replication experiments were performed at C-CORE. All experiments were conducted with silica sand Type '0' with internal friction angle equal to 32° and weight of 13880 N/m^3 when loosely deposited. The 1 m square tank apparatus constructed for experiments in Section 3.1 was used. The same mechanical drive arm was employed for horizontally translating the 60 mm diameter plastic model structure. The structure was vertically supported by two cantilever load cells and, when translated, maintained a constant clearance of 4 mm with a sandpaper-covered false floor. All tests were conducted at 6 mm/s.

"Sand keels" were constructed by placing piles of loose sand across the tank floor in front of a model structure. Precise shaping was achieved using plywood trowels cut out to the shape of the ridge keels profiled in the McKenna *et al.* (1995b) "PWC" study. The trowels were dragged over the loose piles, creating the desired prismatic keel form. The

average profile reported for each of the six ridges and adjusted for the position of the cone was used. Sand was mixed and consistently replaced before each experiment to maintain a consistent density. A total of eleven ice interaction tests were performed in McKenna *et al.* (1995b), two for each ridge except for ridge number five in which only one ice interaction experiment was performed. Eight of these are considered in this study. The "cone low" experiments are omitted because the cone extends down into the keel so that the integrity and shape of the keel portion interacting with the cylinder are more likely to be disturbed.

5.1.3 Experimental results

Force traces for all eight tests have been normalized by peak force and plotted in Figures 5.2 to 5.9. Also plotted are the keel profile and force trace for the corresponding ice ridge interaction experiments. The horizontal position of the ice ridge force traces (relative to the keel) was based on the positioning reported in McKenna (1995b). The horizontal position of the sand traces in the figures was established by shifting them until the start of force increase coincided with that of the ice ridge. This procedure was required since the two force curves were not in phase, perhaps a result of the forward displacement of the ice ridge keels during interactions. Doing so improved the clarity (and probably the positional accuracy) of the superimposed curves. Although force traces may not be in proper phase position with the keel profile, the horizontal scale is correct and so one can easily make correlation observations.

In general, sand and ice force trace patterns are quite similar. The exceptions are that sand force traces are typically less steep on the decline (trace RHS) and have a broader peak than ice force traces. Also ice force traces are characteristically bi-modal when the

keels are this way. Some of these differences can be accounted for by assuming that in the ice ridge experiments very little surcharge develops during interactions at medium and high speeds[1]. If displaced ice blocks are not settled enough to create a surcharge one may expect the force traces to follow the contours of the original undisturbed keel form. Dynamic model scaling is in no way achieved in the sand tests so that a very different fluid dynamic regime exists. Displaced sand which accumulates and flows around the structure settles immediately and provides an instantaneous surcharge. Thus one would expect higher relative loads particularly after the peak where ploughed sand may obstruct the structure even after leaving the original ridge site.

It appears that at high speeds an even greater disparity exists between sand and ice force traces. The most notable dissimilar trace was that for the high speed test PWCPEI1-1 where the trace appeared to be "eroded" over the first half of the curve. This may be the result of the *suspension* of previously undisturbed submerged ice rubble blocks. Fluid accelerating around the advancing structure may shear off ice blocks on the outer surface of the keel in the steepest flow gradient regions. Flow speeds easily exceed that which is critical for the suspension of ice blocks in the PWCPEI experiments (block terminal speed is around 0.26 m/s). At very high speeds engaging blocks may be analogous to spooning tea leaves in a stirred-up cup.

Evidently, the best force trace match is that for the slowest interaction speed (PWCPEI3-2) which lends support to the transient surcharge assumption. For that test the bi-modal keel is not reflected in the ice force trace as prominently as in others at medium speed,

---

[1] This appears to be consistent with video records taken during IMD tests. Fluid dynamic considerations supporting this assumption are also discussed later in Chapter 7.

including PWCPEI3-1 for the same ridge. The slope matches that of the sand where it was observed that ploughed material ahead of the advancing structure had settled into the keel trough.

Generally, ice force traces are more jagged than sand traces. Although, seemingly smooth sand does tend to fail in "blocks", the ice ridge trace has a higher frequency failure mode which may be a feature of a different compressibility and the failure of cohesive freeze-bonds. These effects do not appear to substantially influence the general similitude of patterns.

5.1.4 Conclusions

The force traces from "sand keel" indentation experiments appear to be representative of those for ice rubble interactions over a limited range of interaction speeds. The suitability of results from all sand tests must be considered in light of this sensitivity. The success of modelling ridge keels with sand here, and in Chapter 3, presents an opportunity for more advanced experiments described in following sections.

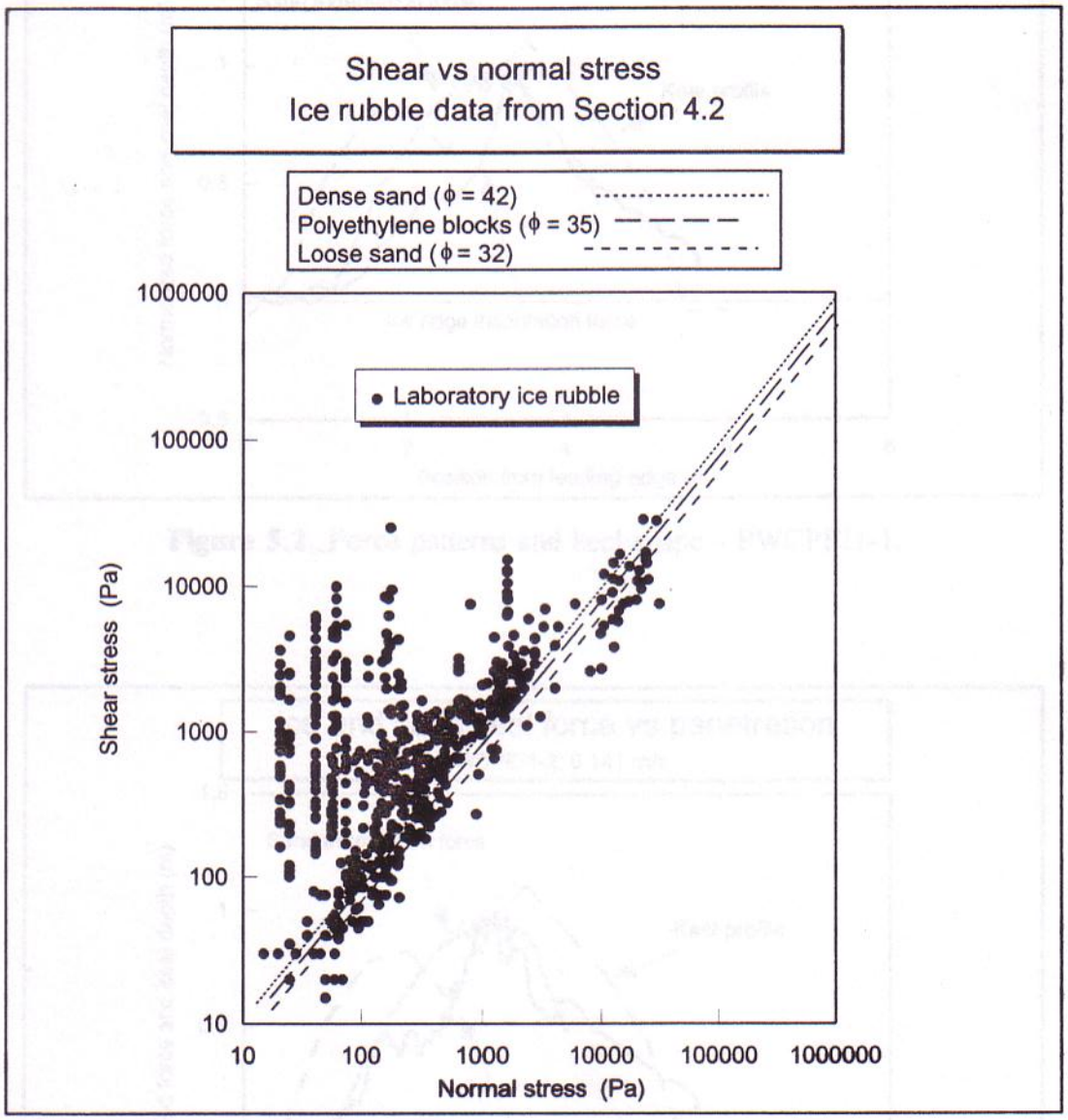

Figure 5.1 Shear vs normal stress: ice rubble, sand, and plastic blocks.

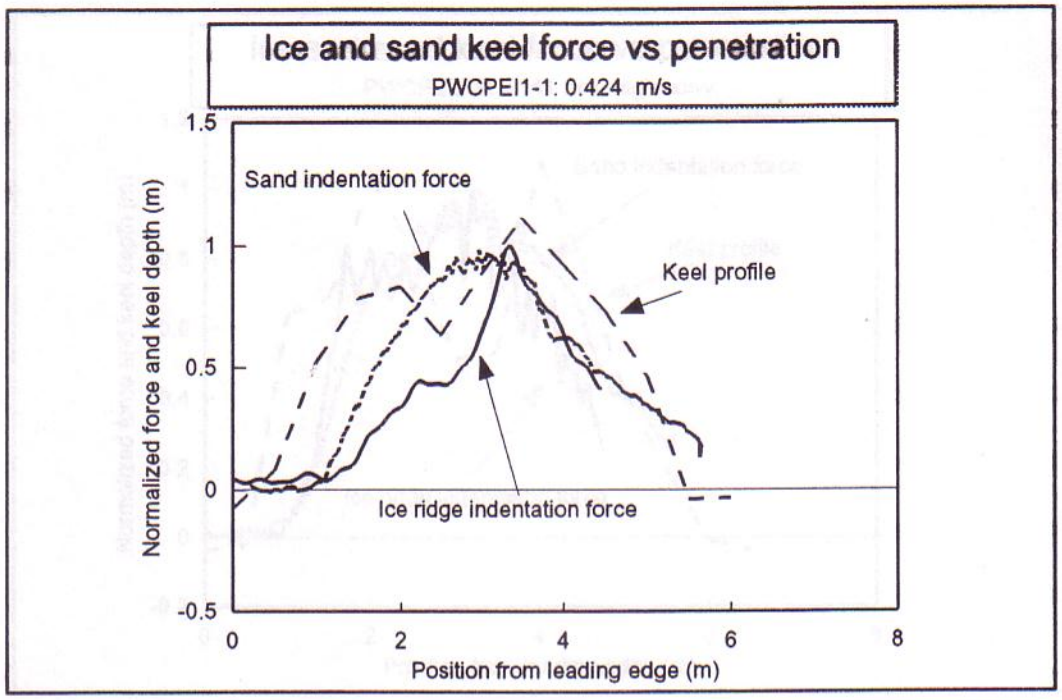

Figure 5.2 Force patterns and keel shape - PWCPEI1-1.

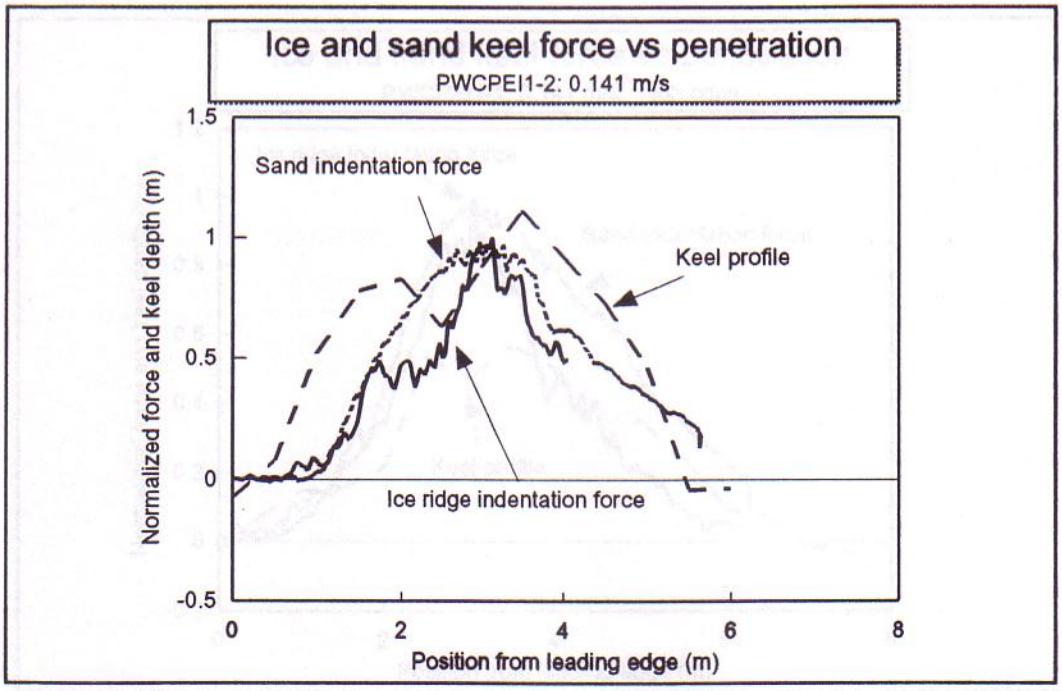

Figure 5.3 Force patterns and keel shape - PWCPEI1-2.

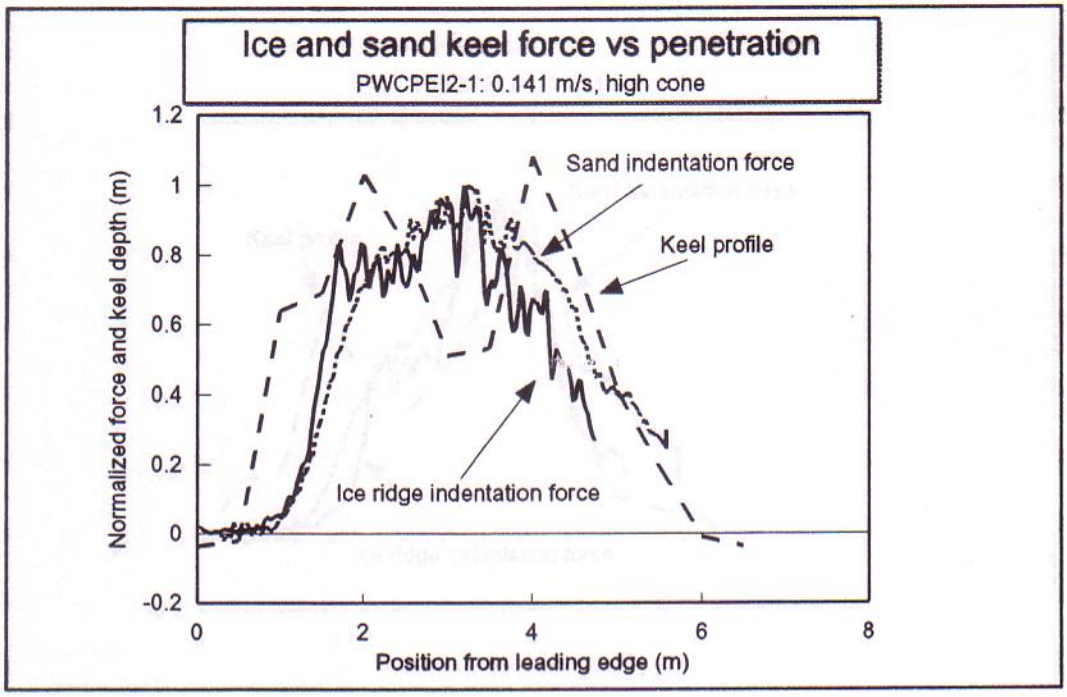

Figure 5.4 Force patterns and keel shape - PWCPEI2-1.

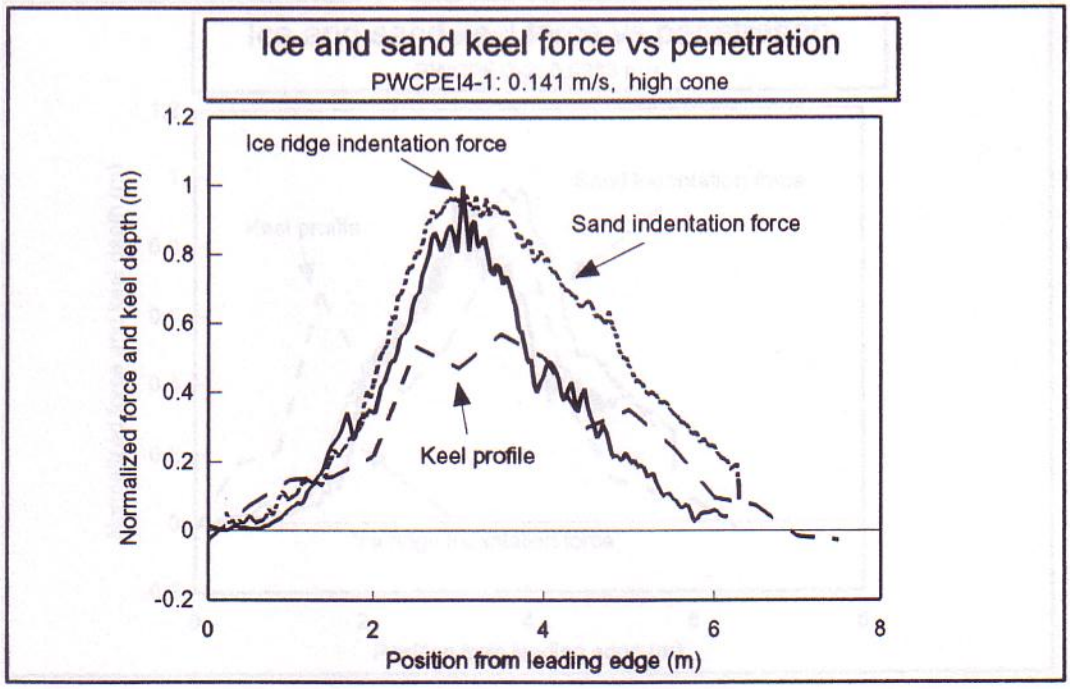

Figure 5.5 Force patterns and keel shape - PWCPEI4-1.

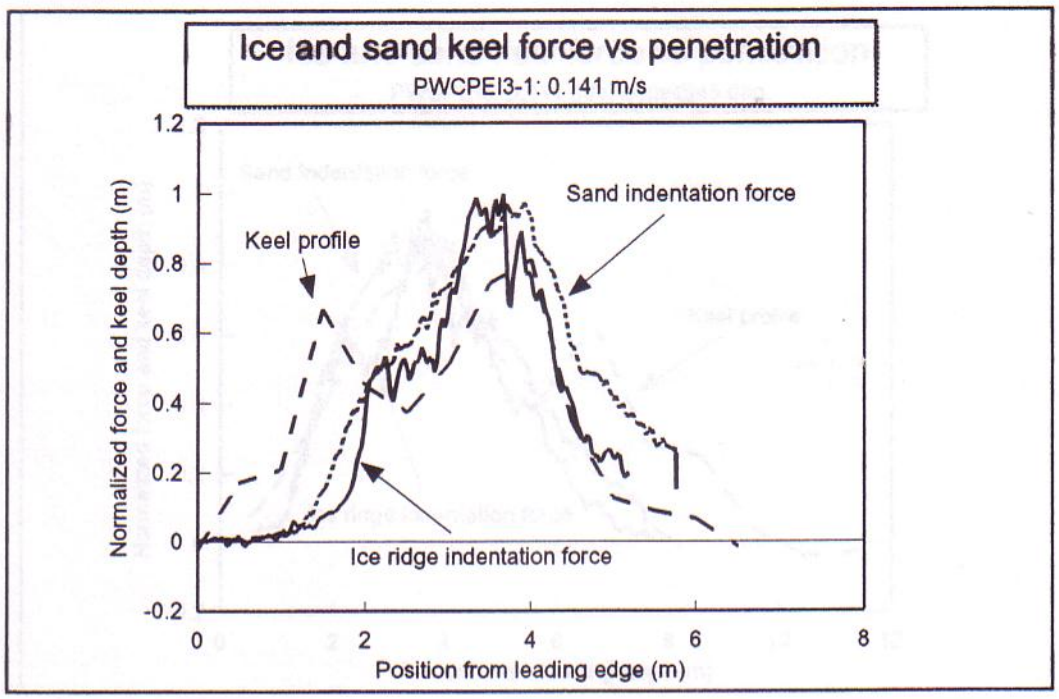

Figure 5.6 Force patterns and keel shape - PWCPEI3-1.

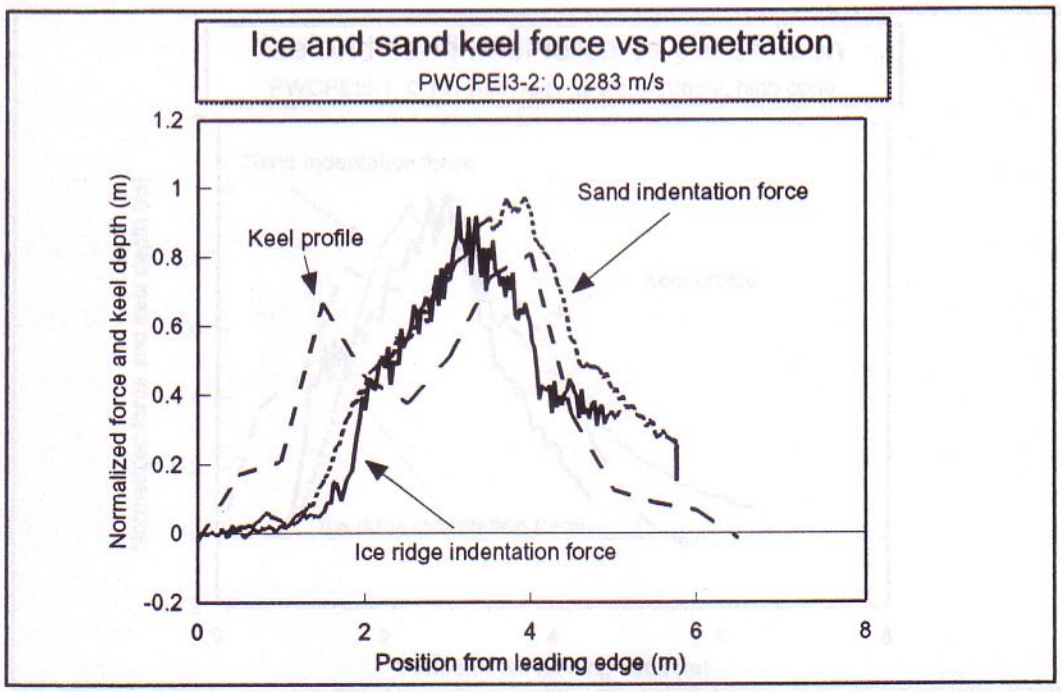

Figure 5.7 Force patterns and keel shape - PWCPEI3-2.

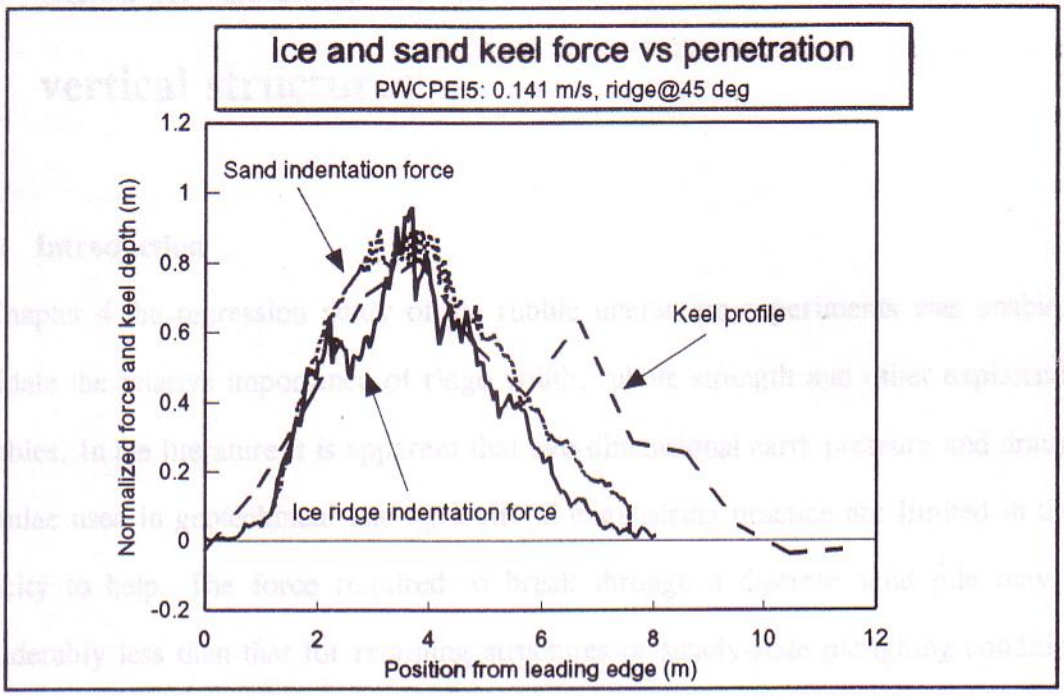

Figure 5.8 Force patterns and keel shape - PWCPEI5.

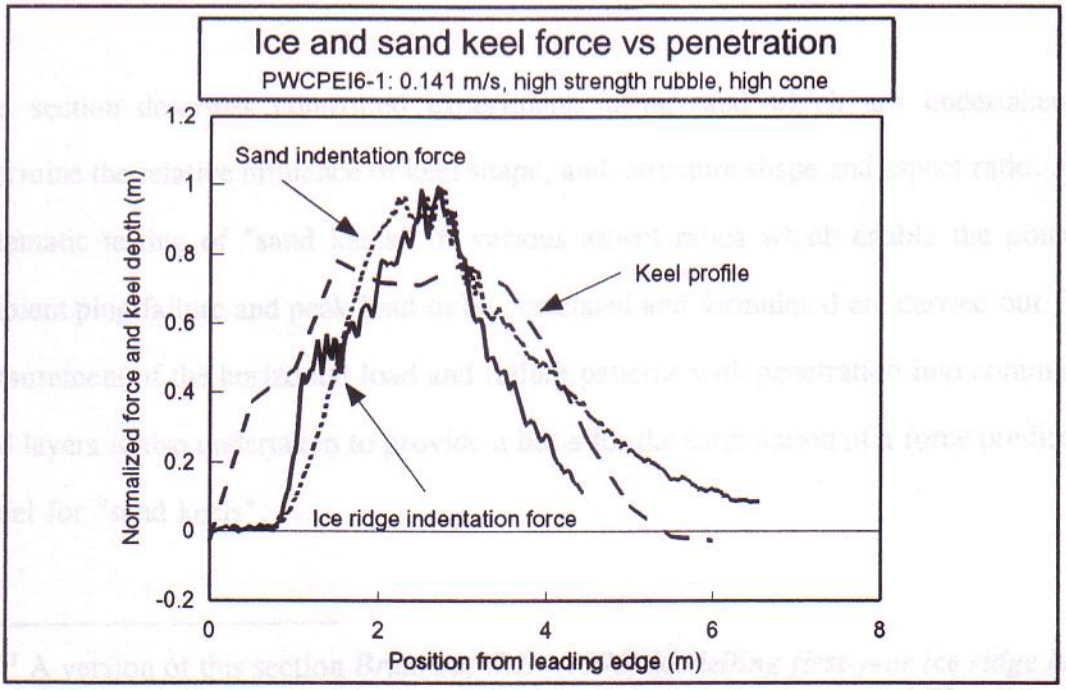

Figure 5.9 Force patterns and keel shape - PWCPEI6-1.

5.2 Sand-modelling of ice rubble forces on vertical structures[1]

5.2.1 Introduction

In Chapter 4 the regression study of ice rubble interaction experiments was unable to elucidate the relative importance of ridge width, rubble strength and other explanatory variables. In the literature it is apparent that two-dimensional earth pressure and draught formulae used in geotechnical and agricultural engineering practice are limited in their capacity to help. The force required to break through a discrete sand pile may be considerably less than that for retaining structures or steady-state ploughing conditions for a continuous horizontal layer. Also the indentation of keels is more complicated than passive pressure on retaining walls because a non-linear, transient surcharge may develop and clearing processes are activated.

This section describes controlled experiments using sand which are undertaken to determine the relative influence of keel shape, and, structure shape and aspect ratio. Also systematic testing of "sand keels" of various aspect ratios which enable the point of incipient plug failure and peak load to be correlated and formulated are carried out. The measurement of the horizontal load and failure patterns with penetration into continuous sand layers is also undertaken to provide a basis for the formulation of a force prediction model for "sand keels".

---

[1] A version of this section ***Bruneau, S.E. (1996) Modelling first-year ice ridge keels with sand***, has been presented at the 49th Geotechnical Conference of The Canadian Geotechnical Society, Sept. 1996, St. John's, Nf.

5.2.2 Experimental program

Experiments were carried out using the same apparatus and similar testing procedures as described in Sections 3.1 and 5.1. Several additional plastic model structures and plywood "keel" trowels were constructed. Refer to Appendix C for a full listing of experimental conditions for all sand tests reported in this section.

For structures indenting symmetrical trapezoid keel formations dimensional analysis yields:

$$\frac{F}{\gamma H^2 D} = f\left[\alpha,\ \delta,\ \phi_1,\ \phi,\ \frac{W}{D},\ \frac{H}{D},\ \frac{P_{en}}{D}\right] \qquad (54)$$

where F is horizontal force, γ is bulk weight, α is the slope of the structure, δ is soil surface slope, ϕ_1 is the soil-structure friction angle, ϕ is the angle of internal friction, W and H are the "sand keel" width and depth, D is the structure projected width and P_{en} is structure penetration from the "sand keel" leading edge. For tines indenting soil there is a critical depth aspect ratio (rubble depth to structure width) above which material is displaced forwards, sideways and upwards, and below which no upward movement occurs. Reported values for the critical depth aspect ratio vary widely with a median value around 7 (Godwin and Spoor, 1977). This study is aimed at applications where aspect ratio is typically no greater than 3, remaining above the critical depth.

5.2.3 Experimental results

Figure 5.10 illustrates the relative influence of "sand keel" shape on peak load and penetration at peak. All five keels (shown beneath the bar graph) had the same sectional

area and two different widths were used. Loads were normalized against the 320 mm-wide trapezoid "sand keel" because it resulted in the highest load and was also the preferred default shape in subsequent tests. Generally, the wider shorter keels resulted in lower loads and significantly greater penetrations at peak. There was little difference between the loads on keels of similar width.

Figures 5.11 and 5.13 illustrate the influence of structural shape on peak indentation force for both trapezoidal "sand keels" and for a continuous sand layer (steady-state loading achieved). Each model shape (shown in Figure 5.11) had the same projected frontal width. The load on the circular cylinder was used to normalize loads for the trapezoidal indentation tests and the square section was similarly used for the continuous layer tests because each produced the respective maxima. The results which show little variation for trapezoidal indentation and moderate differences for continuous layer indentation are in stark contrast to the substantial variation in drag of similar, two-dimensional bodies in a fluid. Force traces for the three structure shapes are superimposed on Figure 5.13. That for the square section has the steepest incline whereas the force trace for the triangular structure is the most gradual.

To establish the quantity of load attributable to "edge effects" flat vertical structures of width D, $2D$, and $3D$ were translated through "sand keels". Peak indentation force for each test was normalized against that for the structure of width D (Figure 5.12). By extrapolating to the normalized force intercept, one obtains a force at an effective width of zero. In this study the edge effect force was 50% of the total indentation force for the structure of width D where the keel was $2.8D$ wide and $2/3D$ deep. Thus, the *effective* width of the structure, D_{eff}, was

$$D_{eff} = D\left[1 + \frac{1.5H}{D}\right] \tag{55}$$

which is necessarily limited by critical depth considerations to around $2D$. It is remarkable that if one inverts the aspect ratio coefficient in the above formula it becomes essentially equivalent to Dolgopolov's shape factor reviewed in Section 2.4. Sample force traces for the three widths are plotted in Figure 5.13.

The relative penetration to peak load has been determined for a range of W/D and H/D ratios for vertical cylinders indenting trapezoidal "sand keels" (Figure 5.14). The penetration at peak force may not be independent of structure roughness and sand density, however, these parameters were not varied in this study. Multiple regression techniques were applied to determine the expression

$$\frac{P_{en}}{D} = 0.113\left[\frac{W}{D}\right]^{1.63}\left[\frac{H}{D}\right]^{-0.42} \tag{56}$$

which has a goodness-of-fit adjusted r^2 value of 97%.

Lastly, continuous sand layers were indented until steady state conditions arose. The point at which steady state failure occurred was approximated because it is a cyclic collapse mechanism (as described by Rajaram and Oida, 1992). Forward rupture distance, r, side rupture distance, s, surcharge height at the structure, H_{sur}, and horizontal force were measured at 5 cm penetration intervals for a range of H/D (Figure 5.15). Expressions for r, s, and H_{sur} have been formulated using multiple regression techniques yielding,

$$\frac{H_{sur}}{D} = 0.818 \left[\frac{H}{D}\right]^{0.43} \left[\frac{(P_{en}/D)^2}{(P_{en}/D)^2+(H/D)}\right]^{1.89} \quad (57)$$

$$\frac{r}{D} = 2.01 \left[\frac{H}{D}\right]^{0.609} \left[\frac{(P_{en}/D)^2}{(P_{en}/D)^2+(H/D)}\right]^{1.11} \quad (58)$$

$$\frac{s}{D} = 1.39 \left[\frac{H}{D}\right]^{0.554} \left[\frac{(P_{en}/D)^2}{(P_{en}/D)^2+(H/D)}\right]^{2.17} \quad (59)$$

with r^2 values (adjusted for degrees of freedom) of 96.5, 98.2 and 92.4% respectively. The basic form of these equations was developed from first principles as described in Appendix D. Patterns of increase and stabilization are the same for all measured quantities. Measurements of r and s required some judgement since rupture form was slightly asymmetric at times and the cyclic formation of leading rupture edges meant that these dimensions ratchetted as the structure advanced.

5.2.4 Development of a load model: cylindrical structures, trapezoidal keels

When a cylindrical structure penetrates a "sand keel", the sand accumulates in a raised crescent around the leading edge with the rupture distance extending further from the structure as surcharge deepens (Figure 5.15). The failure surface is rounded and cusp-like until shear planes, flaring from the structure to the back of the keel, form.

Failure patterns were observed and sketched (Figure 5.13) from time-lapsed photographs taken through a window with a model structure brushing past. For the trapezoidal "sand keel" in Figure 5.13, the failure surface extended upwards at a steep angle from position

0 through to some time after position 1. At that point a transition occurred whereby the sand within the main body of the pile ahead of the structure became fully mobilized. This transition in failure mode appears to mark the point where the classical local passive failure system collapses with the diminished confining stresses at the rear of the pile - promoting an outward instead of upward displacement of sand. In Figure 5.13 it can be seen that this transition between local and plug-like failure also marks the zone in which peak load occurs.

An algorithm for computing peak load requires modelling of only one of the failure modes described above because the point of incipient plug failure is now known from the results in Figure 5.14. Thus, the well established passive earth pressure formula representing the local failure mode has been used and adapted for computing forces in this study as follows:

$$F = \frac{\gamma H_t^2 K_p D_{eff}}{2} \tag{60}$$

where γ is the bulk weight of the sand (measured as 13880 N/m^3), H_t is the total height of sand at the structure ($H_{sur} + H$), D_{eff} is the effective width of the structure, and K_p (from Jumakis, 1984) is the effective passive pressure coefficient defined as

$$K_p = \frac{\cos^2(\phi+\alpha)}{\cos^2\alpha\cos(\alpha-\phi_1)\left(1-\sqrt{\frac{\sin(\phi+\phi_1)\sin(\phi+\delta)}{\cos(\alpha-\phi_1)\cos(\alpha-\delta)}}\right)^2} \tag{61}$$

where α is the slope of the structure, δ is soil surface slope, ϕ_1 is the soil-structure friction angle (0.6ϕ for sand and plastic, after Audibert *et al.*, 1984) and ϕ is the angle of internal friction ($\approx$ 32° for loose sand tested after Paulin, 1992). This formulation is described in more detail in Appendix D.

The average surface slope, δ, was approximated as atan(H_s/2r) by observing in continuous layer indentation that overburden was approximately level over half of the rupture distance before sloping to the toe of the surcharge pile. From the results of experiments here and in Chapter 3 it was concluded that the effects of varying ridge cross-sectional shape, ridge obliquity and structure cross-sectional shape were not great enough to justify inclusion in this force model.

Indentation force has been computed as a function of penetration using two approximations for effective width, D_{eff} (Figure 5.15(d)). The first, method "A", is $D(1+3H/2D) \leq 2D$ from above. Method "B" is an attempt to reconcile the computational procedure with observed failure shape. During local failure the cusp-like wedge of mobilized sand appears to have a uniform vertical cross-section (Figure 5.15). The whole displaced sand body can thus be approximated geometrically by sweeping a vertical wedge of unit width circumferentially at either side of the cylinder projected width. Since the failure surface is approximately straight between the bottom of the structure and the surcharge pile toe, one can integrate the wedge sides and add to the structure diameter as follows:

$$D_{eff} = D + \int_{-\beta}^{\beta} \frac{r}{2}\cos(\theta)\,d\theta = \left(D + r\sin(\beta)\right) \quad ; \quad \beta = atan(s/r) \qquad (62)$$

to get the effective frontal width of the failure surface.

Measured forces are modelled slightly better by method "A" than "B" though both approximations are quite sound. Method "A" matched results with an r^2 value of 96.7% and Method "B" had an r^2 value of 93.2% . The Method "A" D_{eff} is also more appealing than the other owing to its simplicity, not requiring rupture distance values. The peak indentation load for any trapezoidal "sand keel" is obtained from Figure 5.15(d) by determining the penetration at peak for *H/D* and *W/D* from Figure 5.14. Alternatively, the dimensionless formulas for surcharge height, peak force penetration and effective structure width may be used to obtain the same result.

5.2.5 Conclusions

A model of the interaction forces for prismatic structures indenting "sand keels" has been successfully developed and tested. The procedure, based on passive earth pressure, provides a framework for understanding the role of several key explanatory variables. Ridge width, for example, influences the depth of the sand at which peak load occurs. It was not possible to establish this relationship with the ice rubble data sets. The procedures outlined are limited in application to full-scale by an inability to model global inertia, compressibility, fluid dynamic and boundary compliancy effects. The degree to which these effects influence force modelling is investigated, in part, in the following chapters where the procedure developed in this section is applied to ice rubble for load prediction.

With additional sand testing semi-empirical relations for r, s, and H_{sur} may be found for sloping structures including some cones. This is of interest since cones have been used

as ice shields in the Northumberland Strait Bridge Project. Though models for the flexural failure of an ice sheet are well-established, the effects of structure slope on rubble clearing are not well-defined. Analytical solutions similar to those described in this section for vertical structures are possible for cones since conical structures approach cylindrical form with increased slope angle. An alternate modelling procedure may be necessary for cones with a gradual slope.

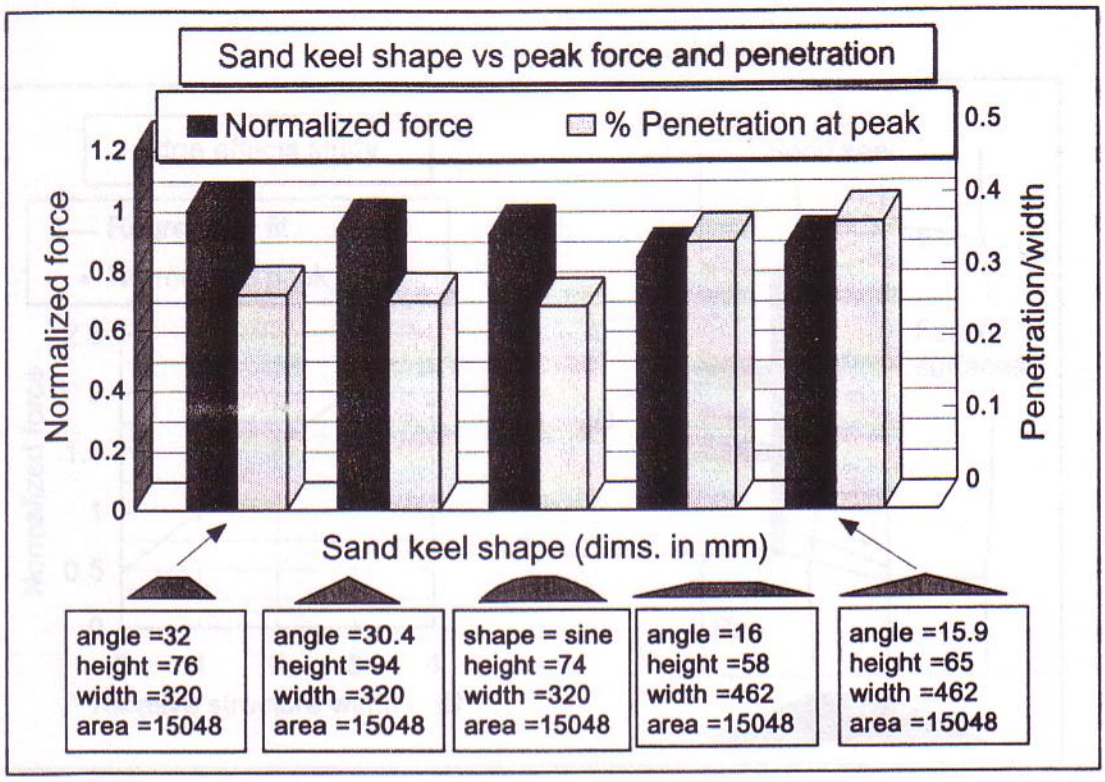

Figure 5.10 "Sand keel" shape study.

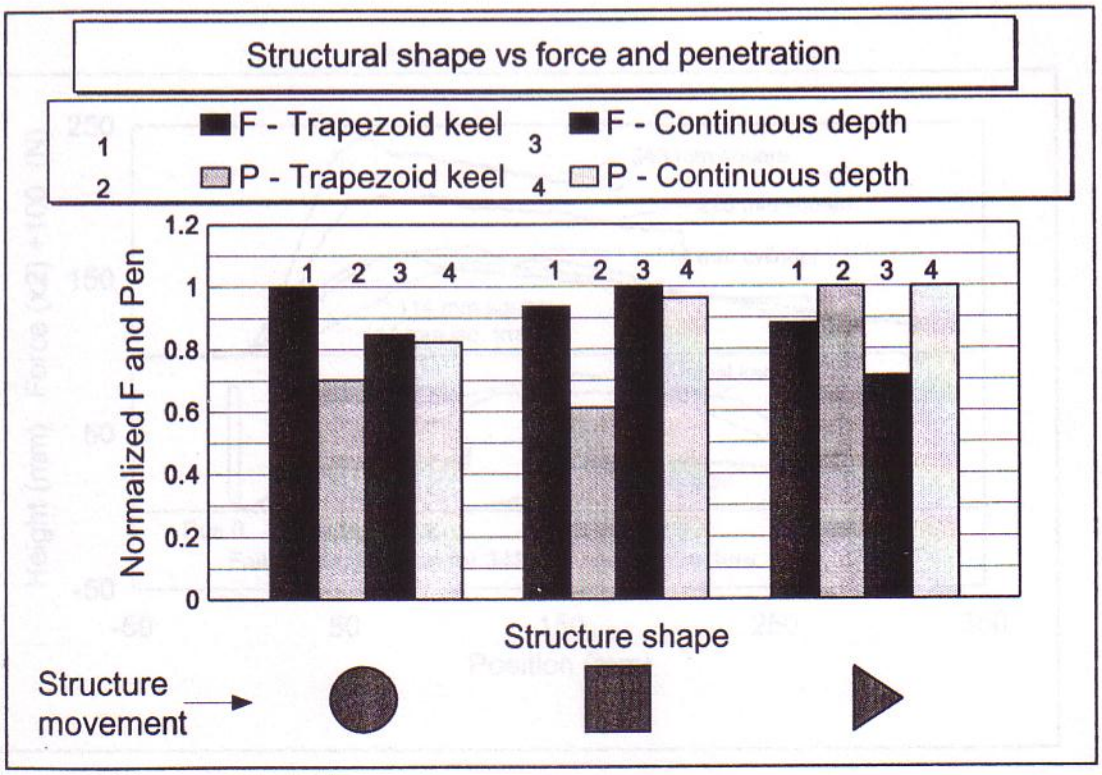

Figure 5.11 Structure cross-sectional shape study.

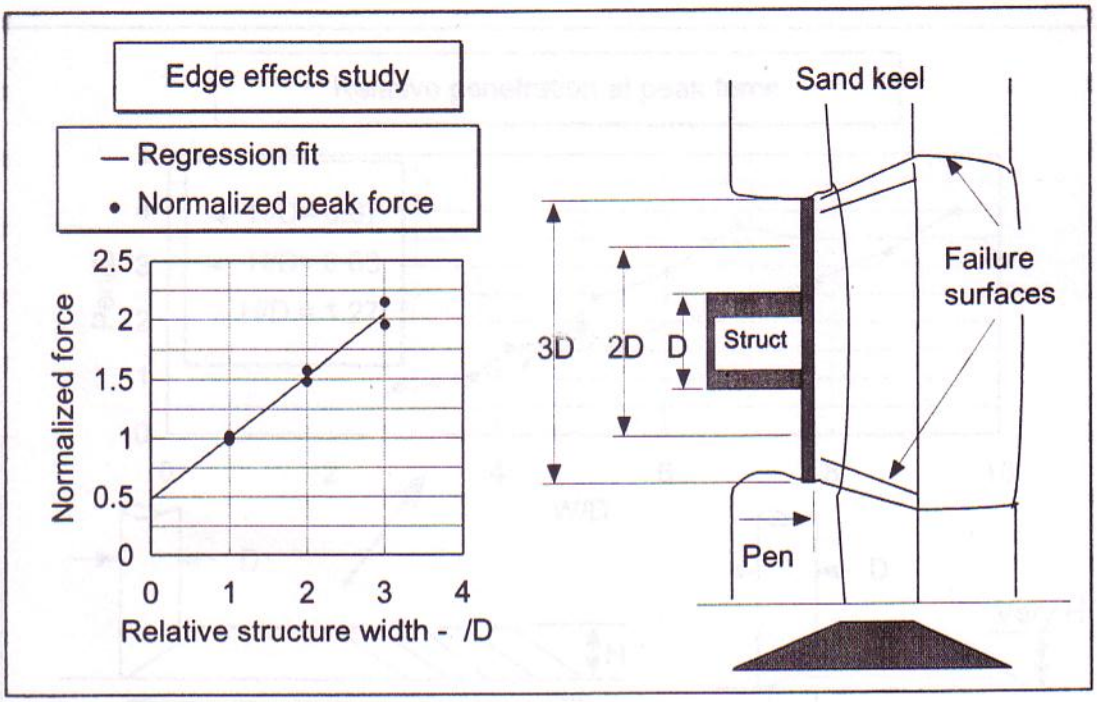

Figure 5.12 Study of edge effects for development of effective width formula.

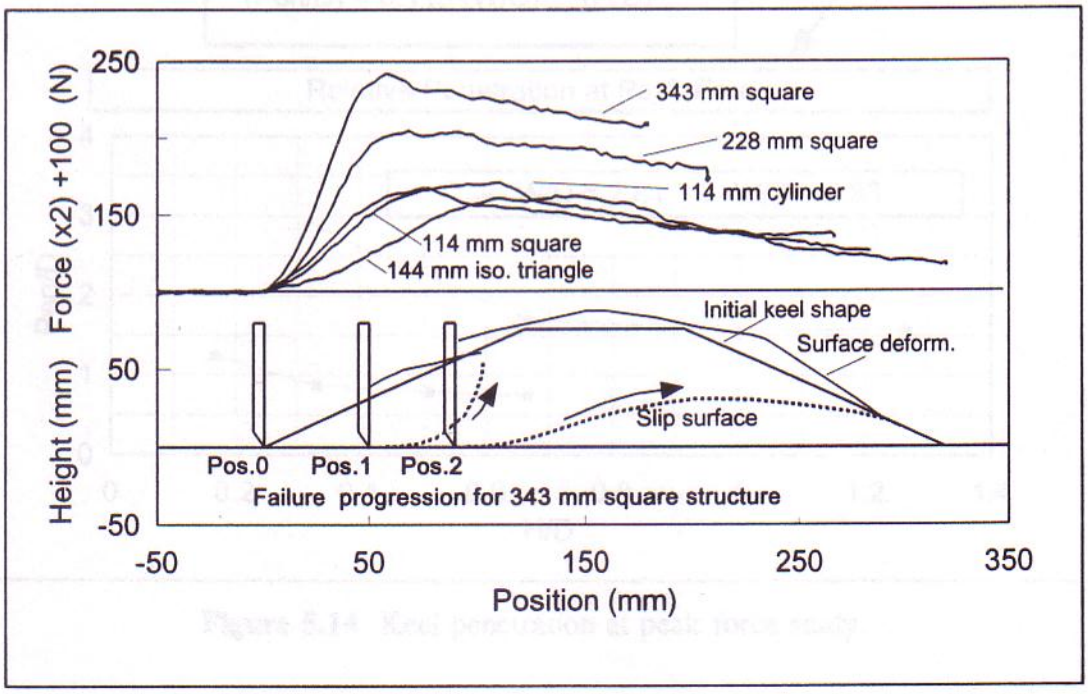

Figure 5.13 Force trace and failure pattern study.

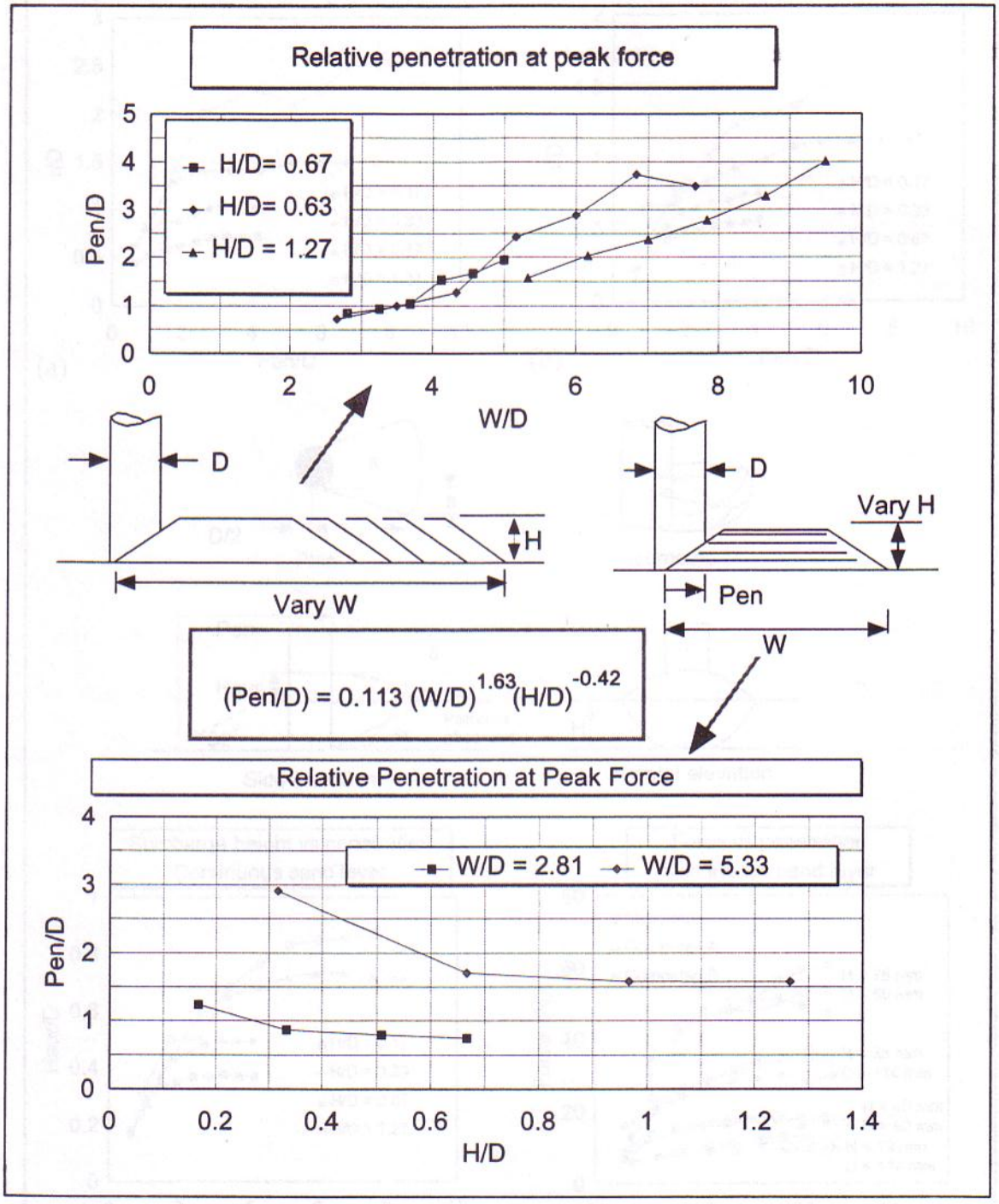

Figure 5.14 Keel penetration at peak force study.

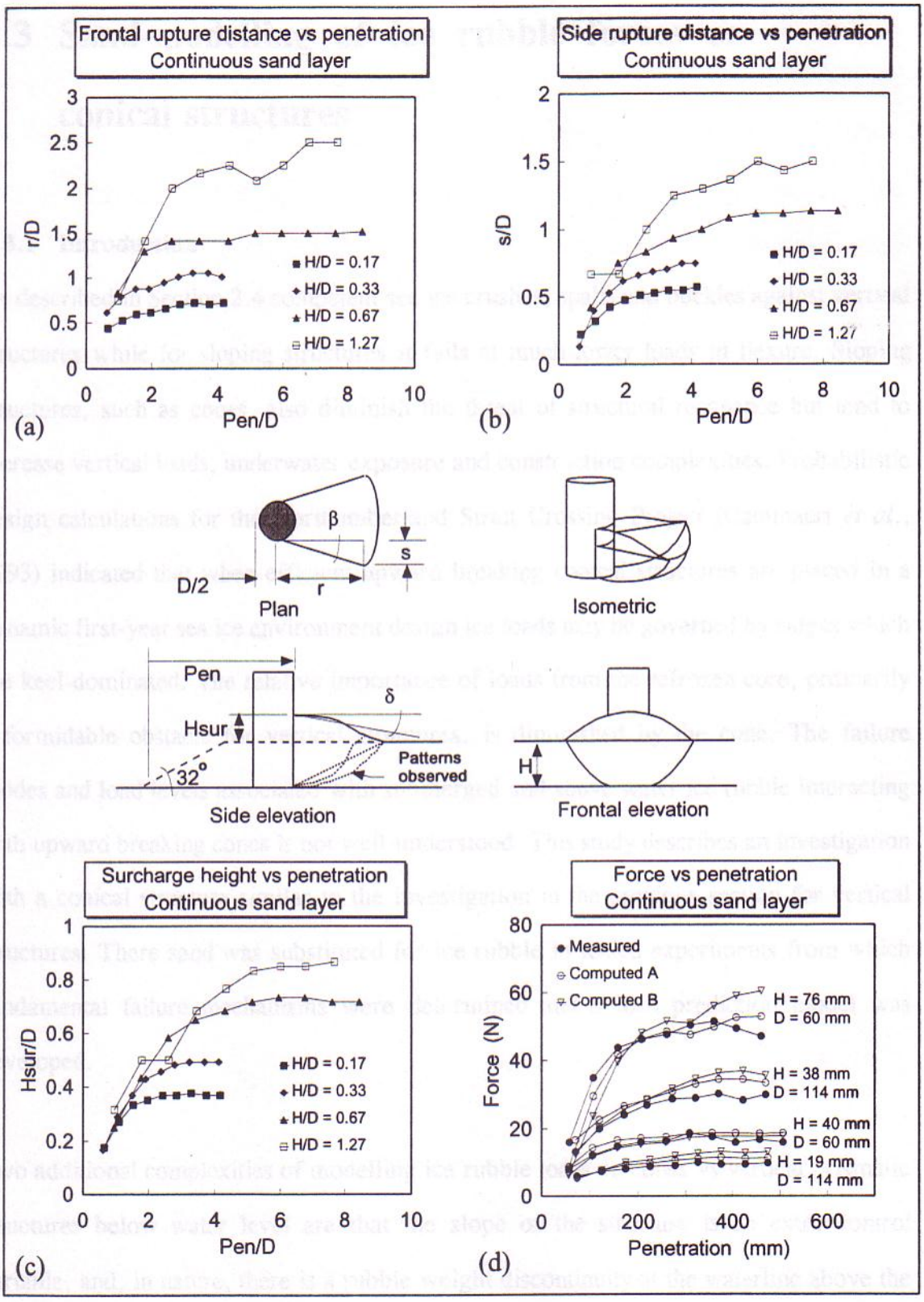

Figure 5.15 Rupture surface evolution, and, measured vs predicted forces.

5.3 Sand-modelling of ice rubble forces on conical structures

5.3.1 Introduction

As described in Section 2.4 competent sea ice crushes, spalls and buckles against vertical structures while for sloping structures it fails at much lower loads in flexure. Sloping structures, such as cones, also diminish the threat of structural resonance but tend to increase vertical loads, underwater exposure and construction complexities. Probabilistic design calculations for the Northumberland Strait Crossing Project (Cammaert *et al.*, 1993) indicated that when efficient upward breaking conical structures are placed in a dynamic first-year sea ice environment design ice loads may be governed by ridges which are keel-dominated. The relative importance of loads from the refrozen core, ordinarily a formidable obstacle for vertical structures, is diminished by the cone. The failure modes and load levels associated with submerged and above water ice rubble interacting with upward breaking cones is not well-understood. This study describes an investigation with a conical structure similar to the investigation in the previous section for vertical structures. There sand was substituted for ice rubble in scaled experiments from which fundamental failure mechanisms were determined and a load prediction model was developed.

Two additional complexities of modelling ice rubble loads on cones vs vertical prismatic structures below water level are that the slope of the structure is an extra control variable, and, in nature, there is a rubble weight discontinuity at the waterline above the base of the cone. In this study only one cone slope was tested (55.7°) and there was no

water present. The failure mode examined in these experiments is thus analogous to ice rubble failure only when upward sloping structures lift rubble and when downward sloping structures depress it. For instance, in cases where upward and downward rubble failure occurs on a single continuous sloping structure (such as a steep cone extending well below sea level) these experiments may not be applicable unless the two failure modes can be treated separately. In the cases where the waterline passes through the rubble bearing on the conical structure and a discontinuity in the confining stress gradient exists, an approximation of effective stress may be required.

5.3.2 Experimental program

Tests were conducted to determine the sensitivity of indentation force and penetration to keel shape. Also, the relative penetration at peak force for keels of various aspect ratios and the evolution of load and failure patterns with penetration into continuous sand layers were tested. Experiments were performed with similar procedures and equipment to those in Section 5.2. For a full listing of test conditions refer to Appendix C.

For conical structures indenting symmetrical trapezoid keel formations dimensional analysis yields:

$$\frac{F}{\gamma H^2 D_{av}} = f\left[\alpha,\ \delta,\ \phi_1,\ \phi,\ \frac{W}{D_{av}},\ \frac{H}{D_{av}},\ \frac{P_{en}}{D_{av}}\right] \qquad (63)$$

where F is horizontal force, γ is bulk weight, α is the slope of the structure, δ is soil surface slope, ϕ_1 is the soil-structure friction angle, ϕ is the angle of internal friction, W and H are the "sand keel" width and depth, D_{av} is the average cone diameter over H, and P_{en} is structure penetration from the "sand keel" leading edge.

5.3.3 Experimental results

Figure 5.16 illustrates the relative influence of "sand keel" shape on peak load and penetration at peak as in Section 5.2. All five keels (shown beneath the bar graph) had the same sectional area and two different widths were used. Loads were normalized against the 320 mm wide "sine" shaped "sand keel" because it resulted in the highest load. The wide short trapezoidal keel showed the least resistance to indentation. There was little difference between the loads on keels of similar width.

The relative penetration of the leading edge of the cone to the position of peak load has been determined for a range of W/D_{av} and H/D_{av} ratios (Figure 5.17). Multiple regression techniques were applied to determine the relation ($\mathbf{r}^2 = 78\%$):

$$\frac{P_{en}}{D_{av}} = 0.57 \left[\frac{W}{D_{av}}\right]^{0.723} \left[\frac{H}{D_{av}}\right]^{-0.0471} \qquad \textbf{(64)}$$

which enables one to interpolate the approximate point of peak load for interaction with keels of various aspect ratios.

Continuous sand layers were indented as far as the apparatus permitted which approached steady-state conditions. Rupture distances and maximum surcharge heights were measured for lateral, forward and oblique (45°) positions around the cone as shown in Figures 5.18 to 5.20. Measurements were made at 5 cm penetration intervals so as to track the development of these parameters and three different sand depths were used. Rupture distances were measured relative to the cone neck and surcharges were measured from the cone base to the top of the sand on the cone. The leading sand pile often crested higher a small distance from the cone surface so the height at that point was recorded.

Multiple regression techniques were used to define longitudinal rupture distance, r_o, and the maximum sand height on the cone, H_{t0} in dimensionless forms as follows:

$$\frac{r_o}{D_{av}} = 0.535 + 2.06\left[\frac{H}{D_{av}}\right]\frac{\left[\frac{P_{en}}{D_{av}}\right]^2}{\left[\frac{P_{en}}{D_{av}}\right]^2 + \left[\frac{H}{D_{av}}\right]} \tag{65}$$

$$\frac{H_{t0}}{D_{av}} = 1.59 * \left[\frac{H}{D_{av}}\right]^{0.652}\left[\frac{\left[\frac{P_{en}}{D_{av}}\right]^2}{\left[\frac{P_{en}}{D_{av}}\right]^2 + \left[\frac{H}{D_{av}}\right]}\right]^{1.07} \tag{66}$$

with adjusted r^2 values of 94.1% and 98.4% respectively. Patterns of increase and stabilization were the same for other measured rupture distances and surcharge heights. The development of these equations is reviewed in Appendix D.

5.3.4 Development of a cone load model: trapezoidal keels

When a conical structure penetrates a "sand keel", the sand accumulates in a raised crescent around the leading edge with the rupture distance extending further from the structure as surcharge deepens. The failure surface is more rounded and cusp-like than that for cylinders. Plug failure is evident when shear planes, flaring from the structure to the back of the keel, form. It was shown in Section 5.2 that the point of plug-like failure corresponds to the point of peak load for vertical structures and the same is assumed here. Thus an algorithm for computing peak load need only model the local failure mechanism at the point of incipient plug failure.

The passive earth pressure formula representing the local failure mode was used and adapted for computing forces in this study as follows:

$$F = \frac{\gamma H_{t0}^{2} K_p D_{eff}}{2} \tag{67}$$

where γ is the bulk weight of sand (measured as 13880 N/m^3), H_{t0} is the greatest depth of sand on the cone, D_{eff} is the effective width of the cone structure, and K_p

$$K_p = \frac{\cos^2(\phi+\alpha)}{\cos^2\alpha\cos(\alpha-\phi_1)\left[1-\sqrt{\frac{\sin(\phi+\phi_1)\sin(\phi+\delta)}{\cos(\alpha-\phi_1)\cos(\alpha-\delta)}}\right]^2} \tag{68}$$

is the effective passive pressure coefficient where ϕ is the internal friction angle ($\approx$ 32° for loose sand used), α is the slope of the structure ($\approx$ 34.3° from vertical), ϕ_1 is the soil-structure friction angle (0.6ϕ for sand and plastic), and, δ is the soil surface slope. Ridge keel shape and orientation have been excluded from the formulation because previous experiments here, and in Chapter 3, indicated that these conditions had a minor influence on forces. Refer to Appendix E for the development of the force equation and to the top Figure 5.18 for conventions and parameter definitions.

The average surface slope, δ, was estimated since the surcharge accumulated in a curved form similar to a cosine function between 0 and $\pi/2$. The sectional area of the sand accumulation was approximately $2/\pi(mH_{t0})$. A triangular accumulation with the same height and area provides an estimate of δ as

$$\delta = atan\left[\frac{H_{sur}}{m\,4/\pi}\right] \tag{69}$$

where m is the cone frontal rupture distance defined on the top of Figure 5.18 and H_{sur} is the surcharge height (H_{to} - H).

The effective width D_{eff} of the conical structure was estimated in two ways. The first, method "A", involves adapting the aspect ratio (effective width) formula developed in Section 5.2 for prismatic structures as follows:

$$D_{eff} = D_{av}\left[1+\frac{3H}{2D_{av}}\right] \leq 2 \qquad (70)$$

where D_{av} is the average diameter of the structure below the original sand depth H.

During local failure the raised crescent of mobilized sand appears to have a uniform vertical cross-section (see top of Figure 5.18 "Isometric"). The whole body can thus be approximated geometrically by sweeping a vertical wedge of unit width circumferentially from one side of the cone to the other. Since the rupture surface extends approximately linearly outward from the cone base up to the sand surface, the effective structural width may be approximated as follows: (Method "B")

$$D_{eff} = \int_{-\beta}^{\beta} B\cos\theta\, d\theta \quad ; \quad B = \frac{r_o+D_s/2+D_b/2}{2} \quad ; \quad \beta = asin\left[\frac{r_{45}}{r_o}\right] \qquad (71)$$

where $B\ d\theta$ is the average horizontal projected width of a soil wedge, β is the approximate angle over which the unit wedge is swept either side of the axis of symmetry. Integrating one obtains

$$D_{eff} = 2B\sin(\beta) \qquad (72)$$

Computed forces using both effective width methods predict measured forces quite well as shown in Figure 5.21. This figure includes two measured force traces for each depth. Method "A" slightly under-predicts loads with an average (for both measured traces) adjusted r^2 value of 99.2% while Method "B" both over- and under-predicts with an average r^2 value of 98.8%.

Predicting a peak load for any given trapezoidal "sand keel" starts with predicting the penetration for peak force using Equation (64) with approximate aspect ratios *H/D* and *W/D*. Using Equation (66) the maximum height of sand acting on the cone can then be determined at that penetration. The surcharge slope and effective structure width are then computed from Equations (69) and (70). Forces are then calculated utilizing Equations (67) and (68).

5.3.5 Conclusions

In this section an analytical procedure that predicts forces on conical structures indenting homogeneous "sand keels" is outlined. The study shows an excellent agreement between measured and computed forces. The applicability of the "sand keel" force model to ice force modelling is limited to conical structures with a slope near that which was tested. Also the introduction describes how other failure modes and rubble stress distributions may affect the applicability of results.

In the next chapter the validity of the sand force prediction models for both vertical and sloping structures is tested for ice rubble forces using data from Chapters 3.

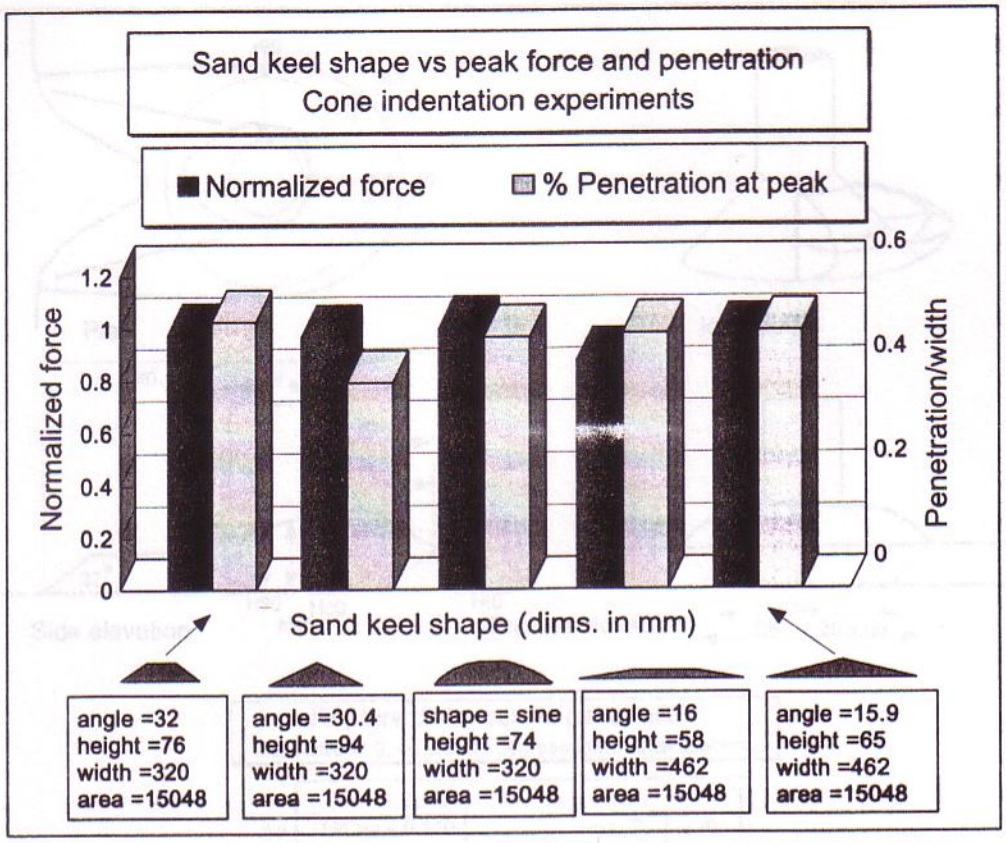

Figure 5.16 "Sand keel" shape sensitivity - cone tests.

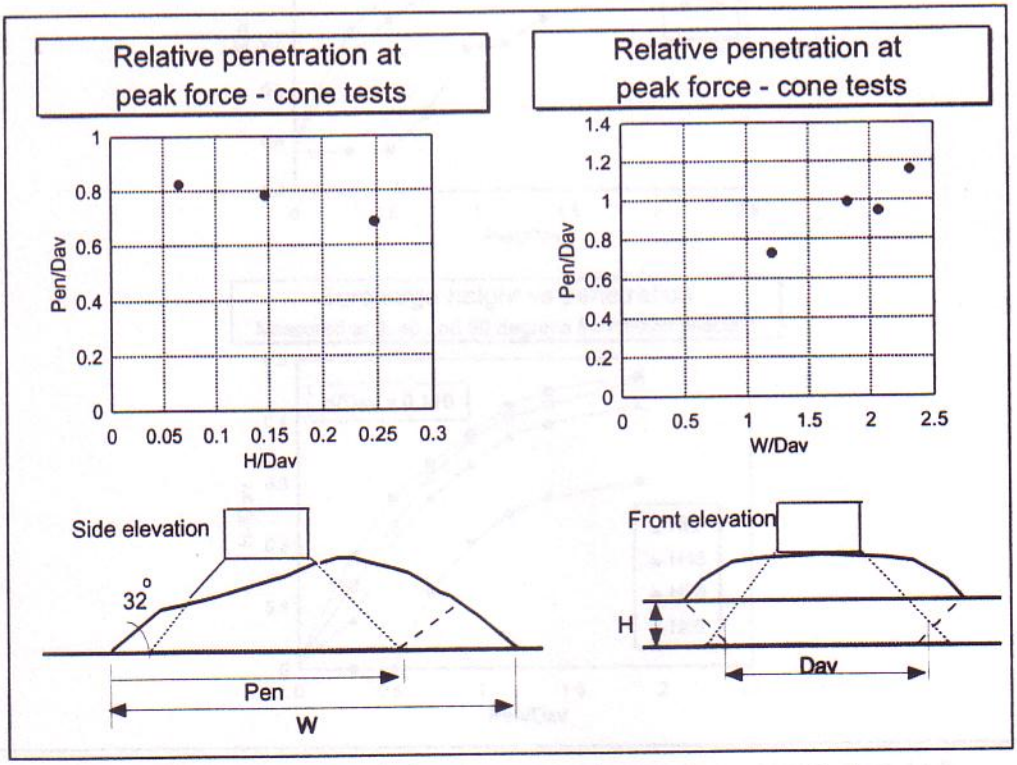

Figure 5.17 Peak force penetration study - cone tests.

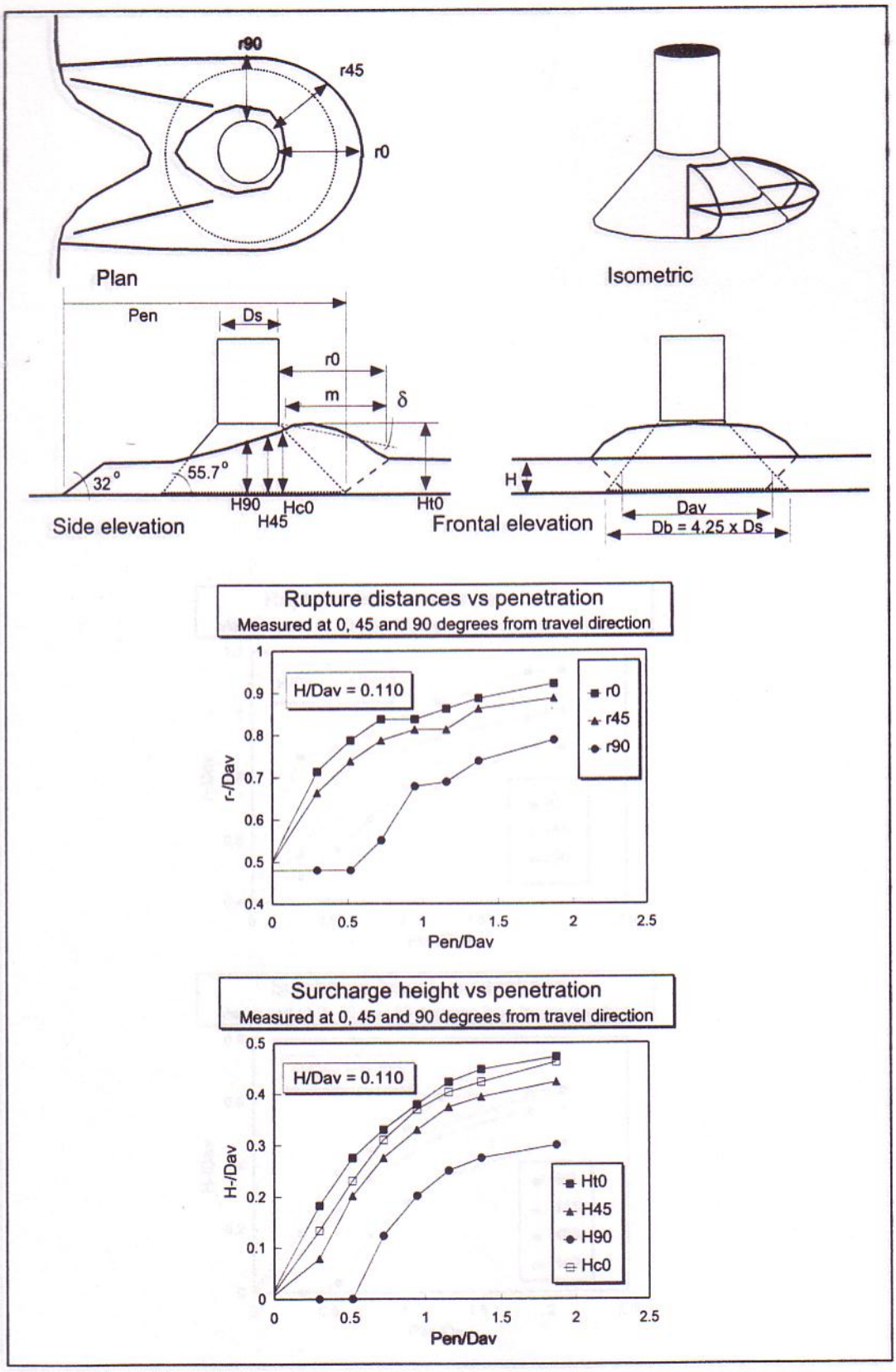

Figure 5.18 Failure patterns for cone penetration - $H/D_{av} = 0.110$.

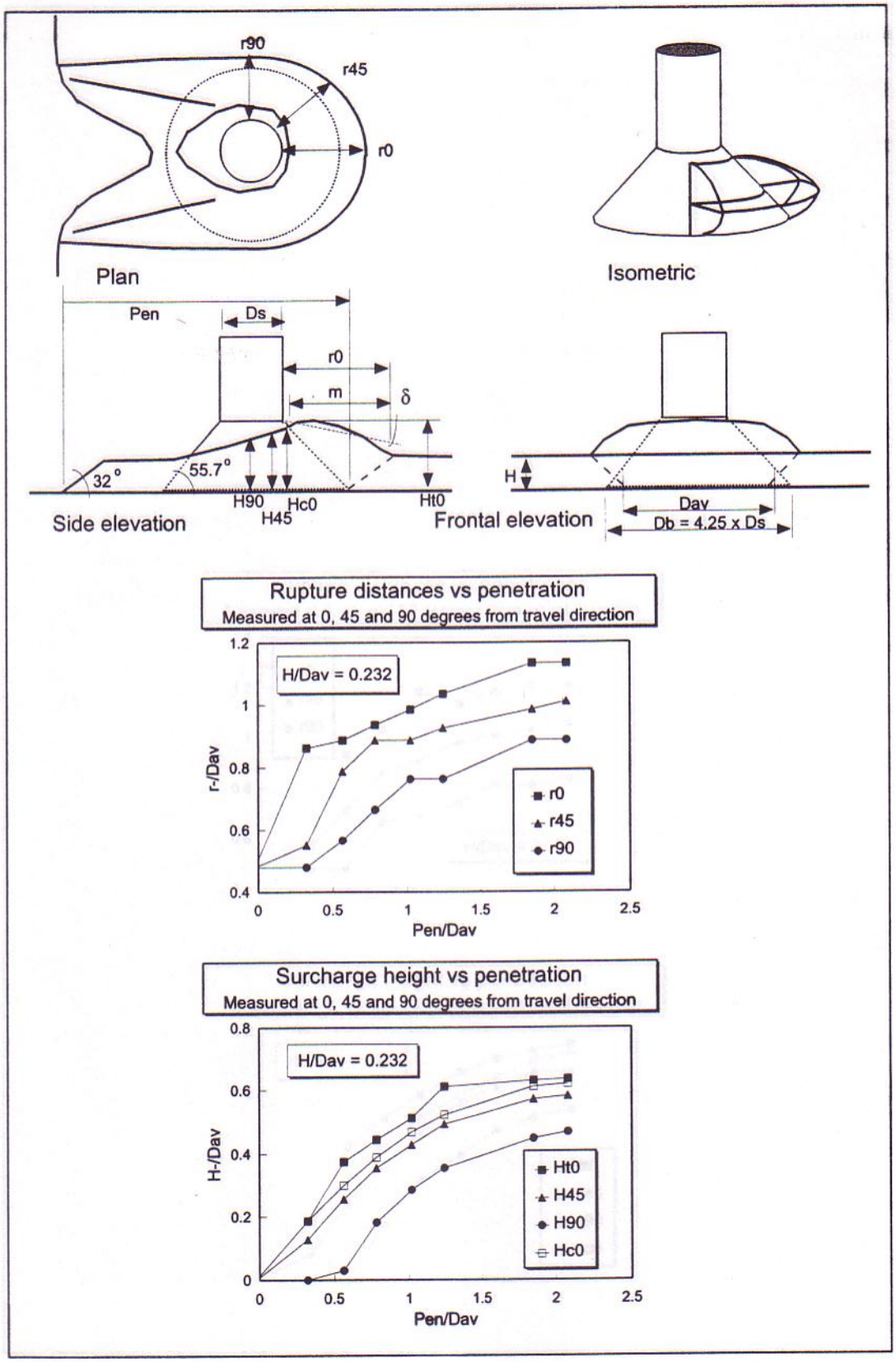

Figure 5.19 Failure patterns for cone penetration - H/D_{av} = 0.232.

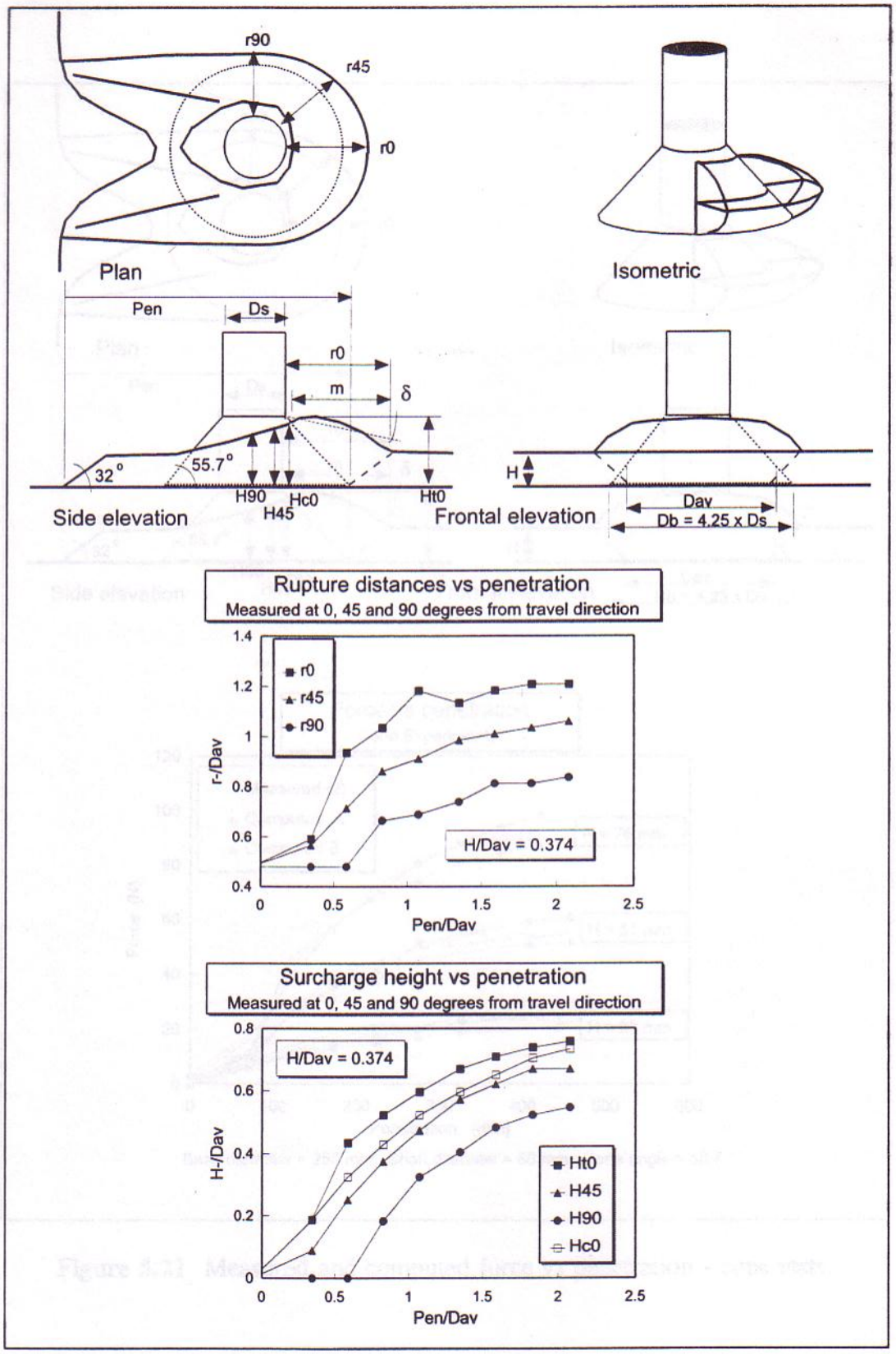

Figure 5.20 Failure patterns for cone penetration - H/D_{av} = 0.374.

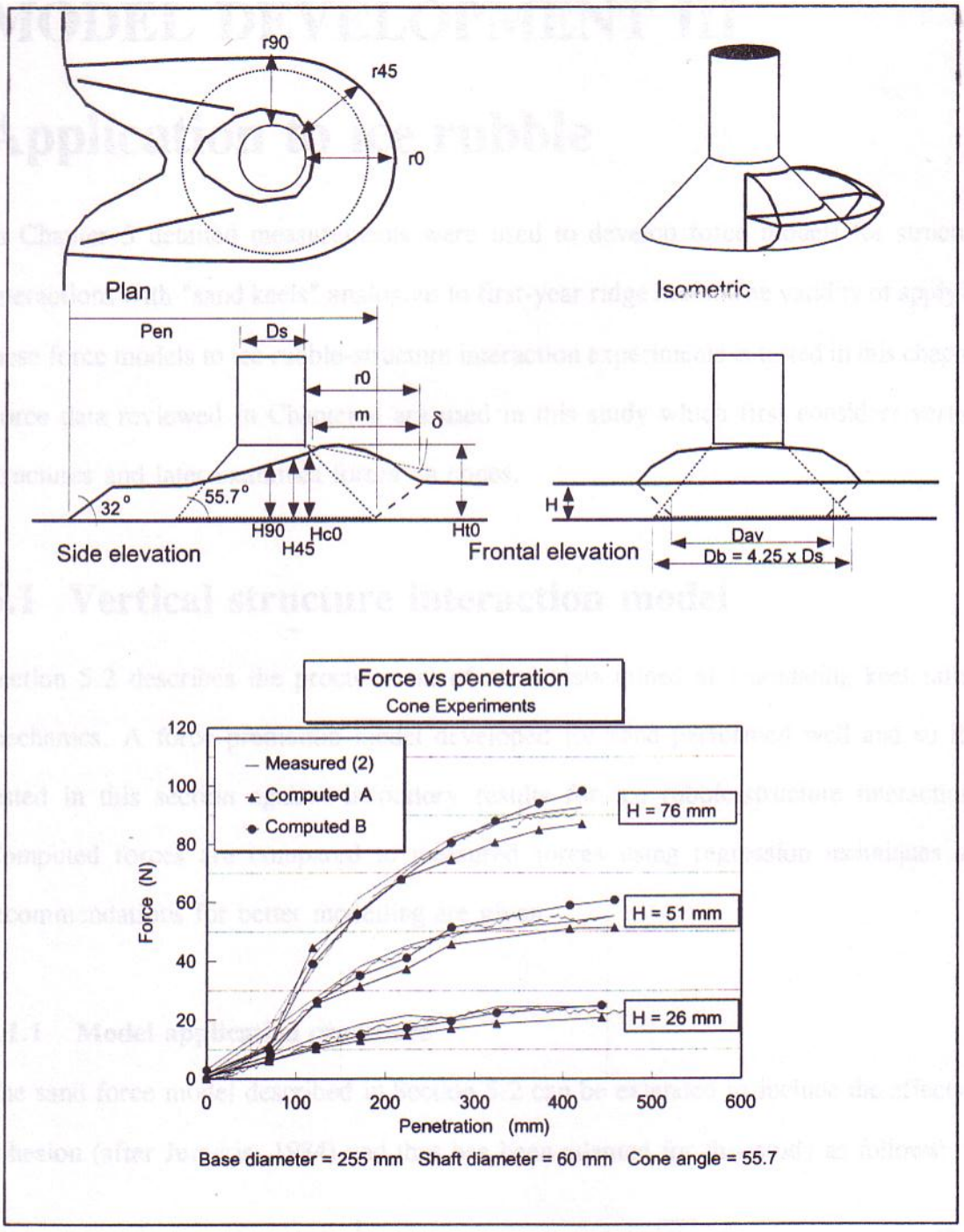

Figure 5.21 Measured and computed force vs penetration - cone tests.